submitted to *Geophys. J. Int.*

# Measuring Higher-Mode Surface Wave Dispersion Using a Transdismensional Bayesian Approach

H. Xu[1], C. Beghein[1]

[1] *Department of Earth, Planetary, and Space Sciences, University of California Los Angeles, Los Angeles, CA* 90095*, USA*

**SUMMARY**

In this paper, we present a novel method for measuring the dispersion of higher mode surface wave phase velocities from a single seismogram using a transdismensional Bayesian approach. The 1-D shear velocity profiles between sources and seismic stations are regarded as the controlling parameters to tune the phase velocities of fundamental and higher modes. The misfits between synthetics and real waveforms indicate whether the phase velocities are recovered well from the data. We use Monte Carlo Markov chains (MCMC) to approximate the posterior distribution of each model parameters, and assess the uncertainties from these probability density functions. While they are time-consuming and computationally intensive, MCMC methods have the advantage of sampling the model space without requiring any explicit regularization other than specifying the bounds of the model space explored. In addition, these techniques can test models of varying dimensions while being parsimonious, thereby letting the data themselves control the complexity of the solution. A reliability analysis inspired by that of Yoshizawa and Kennett (2002) allows us to determine which modes are reliably separated. In this paper, we present the method and first demonstrate its feasibility with a synthetic test, which shows that the technique is robust even when data noise is added. We then illustrate it

with applications to real data. We applied the method to two paths sampling Australia using earthquakes at regional distances, and obtained results that agree well with previous studies. The new method can be used in regional and global tomographic studies to obtain phase velocity maps and 3-D models of seismic velocities and anisotropy at depths that are not well resolved by fundamental mode surface waves or body waves.

**Key words:** Surface waves and free oscillations – Probability distributions – Tomography – Inverse theory – Statistical seismology.

## 1 INTRODUCTION

Higher mode surface waves carry unique, independent constraints on structure at greater depths than commonly used fundamental mode surface waves, and thus enhance the vertical resolution of surface wave tomographic models in the deep upper mantle, transition zone, and uppermost lower mantle. However, most surface wave tomography studies are still limited to fundamental surface waves because traditional surface wave measurements can only be readily applied to fundamental modes and measuring higher modes is complicated. Only in very specific and rare cases has it been possible to isolate and measure the dispersion of the first higher mode Rayleigh wave using single mode dispersion methods (Crampin, 1964; Roult and Romanowicz, 1984). The difficulties in measuring higher modes are mainly due to the fact that their group velocities overlap significantly in a broad frequency range and thus they do not appear as a clear wave train on the seismogram. When distant events are used, a small difference in group velocity can be sufficient to obtain mode separation using numerical techniques, but it is not always enough.

One way to take advantage of the information contained in higher-mode surface waves is to retrieve velocity structure directly, without extracting dispersion curves first. Most of these techniques involve determining path-averaged shear wave velocity structure for multiple station-receiver pairs and combining them to obtain 3-D models of Earth's internal structure. Cara and Lévêque (1987) determined path-averaged $V_S$ models from a single seismogram using mode branch cross-correlation functions (bccf) (Lerner-Lam and Jordan, 1983) as secondary observables. This method, which was designed to minimize the dependence on the starting model, was later automated and combined with a regionalization scheme (Montagner, 1986) to model 3-D velocities (Debayle, 1999) and anisotropy (Maggi et al, 2006). Nolet (1990) developed a two-step non-linear Partitioned Waveform Inversion (PWI) technique that was automated by Lebedev and Nolet (2003). Using synthetic seismogram calculations, the PWI finds along-path velocity models that fit recorded waveforms and inverts the veloc-

ity models obtained for all paths to constrain 3-D structure. Li and Romanowicz (1995; 1996) were also able to obtain the averaged structure along the great circle between the source and receiver using a waveform modeling technique that included non-linear asymptotic coupling theory and coupling across different branches.

Despite the difficulty, several attempts have been made to separate higher modes. Some methods operate in the frequency-wavenumber (w-k) domain and use seismic arrays (Nolet, 1975; Cara, 1973; Cara, 1978; Cara, 1979). While this kind of direct measurement is fast to implement, there are a few limitations: (i) the method can only be applied in regions with dense arrays and thus cannot be applied at the global scale, (ii) it requires the usage of linear regional seismic arrays approximately aligned with the epicenter, which reduces the geographical ray coverage, and (iii) variations within an array cannot be assessed (Laske and Widmer-Shnidrig, 2015).

Another method, based on mode branch stripping, was developed by van Heijst and Woodhouse (1997). The principle behind this technique is that the signals of overtone branches can be isolated by fitting the cross-correlation function of a single mode using mode bccf. However, while this method does not rely on arrays and thus can be used in global tomography, it does not work well with short epicentral distance since individual higher mode cannot be separated from others in a seismogram when the path is not long enough. Additionally, it might be difficult to separate one single mode from observed seismograms when that mode is contaminated by interference from other modes.

Other researchers have utilized waveform fitting techniques to extract higher-mode dispersion. Stutzmann and Montagner (1993) and Stutzmann et al. (1994) developed a waveform fitting technique to invert phase velocity dispersion and velocity structure at depth in successive steps. Beucler et al. (2003) proposed a roller-coaster technique, in which the phase velocity perturbation is obtained by fitting the synthetic seismogram to the real data. Yoshizawa and Kennett (2002; 2004) used the Neighborhood Algorithm (Sambridge, 1999a) to search the model space for multimode dispersion in a nonlinear waveform inversion. Visser et al. (2007) developed a method similar to that of Yoshizawa and Kennett (2002) to estimate multimode dispersion curves for global tomography, though they were additionally able to obtain quantitative uncertainties on the phase speed measurements by performing a Bayesian appraisal of the models sampled (Sambridge, 1999b). Uncertainties were determined from the whole ensemble of dispersion models obtained instead of taking the standard deviation of the 1,000 best models as in Yoshizawa and Kennett (2002).

In our study, we developed a waveform modeling method using a reversible jump Markov Chain Monte Carlo (rj-MCMC) inversion (Bodin and Sambridge, 2009) to extract higher mode dispersion curves and their uncertainties. Like the methods of Yoshizawa and Kennett (2002) and Visser et al. (2007; 2008), our technique has the advantage of sampling the model space instead of choosing one

model among many possible solutions with a strong regularization scheme. It therefore provides more reliable posterior model uncertainties than regularized inversions. Additionally, contrary to Yoshizawa and Kennett (2002) and Visser et al. (2007; 2008) who adopted a fixed dimension model space chosen a priori, the rj-MCMC sampler offers a way to treat the dimension of the model space as variable. In addition, because we use a Hierarchical Bayes approach, data noise parameters are treated as unknown in the inversion, which accounts for the part of the signal that we are not able to explain with our forward theory and the chosen parametrization. In this paper, we first present the method and validate it using a synthetic test, and then show two real data examples.

## 2 METHOD

Our goal is to measure phase velocity dispersion for fundamental and higher mode Rayleigh waves using waveform modeling. To do this, we seek all possible path-averaged 1-D shear-velocity models that can fit the filtered waveform, and the resulting models are employed to calculate dispersion curves. These path-specific 1-D models are not considered to represent the average structure of the Earth along the path, but correspond to a summary of the fundamental and higher-mode dispersion curves for the chosen source-receiver path as in Yoshizawa and Kennett (2002) and Visser et al. (2007; 2008). The procedure we employed to model the waveform is explained in section 2.1 and the rj-MCMC method used to find the 1-D velocity models is explained in sections 2.3 and 2.4.

### 2.1 Waveform Modeling

A synthetic seismogram ($s$) can be calculated as a sum of normal modes ($m$) using the JWKB approximation in the frequency domain ($\omega$) (e.g. Dahlen and Tromp(1998)):

$$s(\omega) = \sum_m A_m(\omega) exp[i\omega\Delta/c_m(\omega)] \quad (1)$$

The relationship between seismograms and their corresponding velocity model is thus highly non-linear. A fully non-linear approach, which does not require any partial derivatives with respect to model parameters or any strong constraints on parameterization, is therefore desirable to perform waveform inversion.

Fortran code Mineos (Masters et al., 2011) can be used to compute synthetic seismograms for a reference 1-D model of Earth's interior by normal mode summation. The advantage of such formulation is that it builds a direct connection between seismic waveforms and phase velocities. However, the calculation of normal mode eigenfunctions and eigenfrequencies for a given mantle model is very time-consuming and thus we cannot use the fully non-linear formulation that is Eq. 1 at each iteration

of a MCMC scheme. We thus decided to linearize the forward modeling problem in order to overcome the speed limitation. As in Yoshizawa and Kennett (2002), we obtained a first synthetic seismogram for a reference model using fully non-linear calculations (Eq. 1). We then used perturbation theory to update the seismogram for other models generated at each iteration of the Markov Chain. For a small perturbation, the change in mode eigenfrequency can be calculated assuming unperturbed eigenfunctions:

$$\delta \ln(\omega) = \int_0^a (\frac{\delta\alpha}{\alpha} K_\alpha + \frac{\delta\beta}{\beta} K_\beta + \frac{\delta\rho}{\rho} K_\rho^{'}) dr + \sum_d \delta d [K_d]_-^+ \tag{2}$$

where $\delta \ln(\omega) = \delta\omega/\omega$, $a$ is the radius of the Earth, and $\alpha, \beta, \rho$ and $d$ are P-wave velocity, S-wave velocity, density, and radius of discontinuities, respectively. $K_\alpha, K_\beta, K_\rho^{'}$ and $K_d$ are the Fréchet derivatives, which relate the change in wave velocities, density, and depth of discontinuity from the reference model to changes in the eigenfrequencies. The Fréchet derivatives can be calculated for each mode using the eigenfunctions determined for the reference model (Woodhouse, 1980). Here, the P-wave velocity and the density are not considered because they have little influence on the phase velocity perturbation in the frequency range we consider (5 mHz - 20 mHz). Hence, Eq. 2 becomes:

$$\delta \ln(\omega) = \int_0^a \frac{\delta\beta}{\beta} K_\beta dr \tag{3}$$

The updated frequency can then be converted into phase velocity for a normal mode of angular order $l$ using (Jeans, 1923; Dahlen and Tromp, 1998):

$$c(\omega^*) = \frac{\omega^* a}{l + 0.5} \tag{4}$$

where $\omega^*$ is the updated eigenfrequency for the mode considered. In Figure 1, we compare synthetic seismograms calculated using the fully non-linear formulation (Eq. 1) and the linearized method described above (Eq. 3). The results show that the phase velocity information from the linearized perturbation method and the non-linear formulation match well, especially in the period range we are interested in (50-200s).

The rj-MCMC method described below performs a guided Monte Carlo sampling of the model space using the values of the misfit between the real and the synthetic seismograms. The data and the synthetics are compared in different time and frequency windows, which are chosen such that they include the fundamental and the higher modes. Table 1 shows a summary of time windows used in this study. We mainly used group velocity to determine the start and end of each window. The letter $b$ in the table indicates that the start time of the window is determined from S- or SS-wave arrival as in Visser et al. (2007). To better fit the waveforms of higher modes, we chose a relative least squares

misfit defined as (Visser et al., 2007):

$$M = \sum_{w=1}^{N} \sum_{i=1}^{L} \frac{(d_i - s_i)^2}{(d_{max}(w))^2} \tag{5}$$

where $d$ is the observed seismogram, $d_{max}$ is the maximum amplitude of the observed data for the window $w$ and s is the synthetic seismogram. The number of time windows is $N$ and the length of each time window is $L$.

### 2.2 Bayesian inference

In a Bayesian formulation, model parameters are described by probability density functions (PDFs), which effectively indicate the uncertainty associated with these parameters. The aim of a Bayesian inference is to quantify the *a posteriori* probability distribution of all model parameters given some prior information and the data. Bayes' theorem (Bayes, 1763) gives the posterior as:

$$p(\mathbf{m}|\mathbf{d}_{obs}) \propto p(\mathbf{d}_{obs}|\mathbf{m})p(\mathbf{m}) \tag{6}$$

where $A|B$ means $A$ given (or conditional on) $B$, i.e. the probability of having $A$ when $B$ is fixed. $\mathbf{m}$ is the vector of model parameters and $\mathbf{d}_{obs}$ is the observed data. The term $p(\mathbf{d}_{obs}|\mathbf{m})$ is called likelihood function, which shows the probability of observing data $\mathbf{d}_{obs}$ given a particular model $\mathbf{m}$. The *a priori* probability of model, $p(\mathbf{m})$, contains what we assume about the model $\mathbf{m}$ before having the observed data. Accordingly, the posterior distribution represents the probability of the model, given the observed data. The parts of the model space that are more frequently required by the data than others manifest with greater posterior probability, and hence are more likely to reflect properties of the Earth (Backus, 1988).

The likelihood function $p(\mathbf{d}_{obs}|\mathbf{m})$ describes the probability of data given the current model. In this study, we assume the noise in the data follows a multivariate normal distribution with zero mean and covariance matrix $\mathbf{C}_d$. The likelihood term is thus written in this form:

$$p(\mathbf{d}_{obs}|\mathbf{m}) = \frac{1}{\sqrt{(2\pi)^n |\mathbf{C}_d|}} \times \exp[-\frac{\Phi(\mathbf{m})}{2}] \tag{7}$$

where $\Phi(\mathbf{m})$ is the function describing the distance between real data and synthetics predicted by the current model. The general expression for $\Phi(\mathbf{m})$ considering correlated noise is (Bodin et al., 2012):

$$\Phi(\mathbf{m}) = (G(\mathbf{m}) - \mathbf{d}_{obs})^T \mathbf{C}_d^{-1} (G(\mathbf{m}) - \mathbf{d}_{obs}) \tag{8}$$

For simplicity, we assume the noise to be Gaussian and uncorrelated, in which case the covariance matrix becomes diagonal. Note that the expression of $\Phi(\mathbf{m})$ then becomes the least square misfit normalized by the diagonal element of $\mathbf{C}_d$, i.e. a $\chi^2$ misfit. As mentioned above, we used the relative

misfit (Eq. 5) instead in order to assign more weights to the higher modes. Hence, the expression for the likelihood is:

$$p(\mathbf{d}_{obs}|\mathbf{m}) = \frac{1}{(\sqrt{2\pi}\sigma_{noise})^n} \times \exp[-\frac{M}{2\sigma_{noise}^2}] \tag{9}$$

where $\sigma_{noise}$ is the standard deviation of the Gaussian uncorrelated noise, i.e., the diagonal element of the covariance matrix. M is a cost function to estimate the data misfit as defined in Eq. 5.

As shown in Eq. 7, the level of noise also accounts for theoretical errors, that is, the part of the signal that we are not able to explain with our forward theory and the chosen parametrization, which is a simplified and discretized representation of the real Earth. Unlike traditional inversion methods in which the noise level is fixed at a presumed level, we use a Hierarchical Bayes approach instead, treating noise parameters $\mathbf{C}_d$ as unknown in the inversion. The diagonal element $\sigma_{noise}$ is given by a uniform prior distribution and will be explored during the Monte Carlo search. This way we avoid arbitrary choice of noise level from the user.

Following Bodin et al. (2012), a uniform prior distribution with relatively wide bounds is adopted here so that the final model will be dominated by the data rather than by prior information. When only independent parameters are considered, the prior probability distribution can be written as the product of three terms:

$$p(\mathbf{m}) = p(\mathbf{c,v}|k)p(k)p(\mathbf{h}), \tag{10}$$

where **c,v** are vectors containing the depth and velocity of each interpolation point, $p(k)$ is the prior on the number of layers, and $p(\mathbf{h})$ is the prior on noise hyper-parameters. Details of the derivation for the expression of $p(\mathbf{m})$ can be found in Bodin et al. (2012). Here, we only show the expression for velocity priors at the $i$th interpolation point $v_i$:

$$p(\mathbf{c}|k) = \begin{cases} \frac{1}{\Delta v} & \text{if } V_{min} \leq v_i \leq V_{max} \\ 0 & \text{otherwise,} \end{cases} \tag{11}$$

where $V_{max}$ and $V_{min}$ are the upper and lower bounds of velocity, and $\Delta v$ is equal to $(V_{max} - V_{min})$. Any velocity that falls outside this pre-defined boundaries leads to a null prior. For our study, we chose $\Delta v = 10\%$ of the velocity in the reference model at a given depth.

### 2.3 The rj-MCMC method

The goal of the rj-MCMC method is to generate an ensemble of Earth models distributed according to a target distribution. In our case, we want to find the 1-D shear velocity models that best fit the waveform data to represent the dispersion of multiple modes along a specific source-receiver path.

Most inversion schemes adopt a fixed dimension model space. However, we do not know the com-

plexity of the $V_S$ profile, i.e. the dimension of the model space, a priori. One potential drawback of fixing the depth parameterization is that different seismograms may require different number of model parameters to improve the fit and the results could potentially depend on the chosen prior parametrization. Here, we adopted a transdimensional Bayesian inversion, which consists in a sampling-based algorithm that include the number of parameters in the set of unknowns and hence the constraints added on the uncertain parameterization or uncertain data errors can be released. The transdimensional approach lets the data themselves constrain the allowable model complexity instead of having the user choose a model parametrization (e.g., number of layers, or cells) a priori. It is well-known, however, that increasing the complexity of the model parametrization often results in better data fit and introduces parameter trade-offs. One difficulty in inverse problems is to determine which parameters are well resolved and how much complexity is really needed by the data. To avoid this problem, the rj-MCMC sampler, first proposed by Geyer and M$\phi$ller (1994), is designed to find a parsimonious solution (Malinverno, 2002), i.e. it naturally discourages high dimensional (many layers) models and the least complex explanation or model for an observation is preferred to avoid over-fitting the data.

The rj-MCMC method has been explained in detail in Bodin and Sambridge (2009) and Bodin et al. (2012). Our method is based on theirs except that we used a different depth parameterization. The nodes in the two different parameterizations have, nevertheless, a similar meaning and the derivations are similar to theirs. The main difference comes from the way the velocity models are constructed. In Bodin et al. (2012), each Voronoi nucleus defines its nearest neighbor region as one layer, which has the same velocity as the nucleus within it. By contrast, in our model the shear wave velocity perturbation at a given depth is interpolated from its two nearby nodes.

In the rj-MCMC method, every new model is generated by iteratively perturbing the last one according to some chosen proposal distribution. There are five types of perturbation based on the parameterization we chose:

(1) Change the velocity of one interpolation point;

(2) Birth: create a new interpolation point;

(3) Death: remove one interpolation point at random;

(4) Move: Randomly pick one interpolation point and move it to a new depth;

(5) Change the noise level;

Here we have employed a slightly different model proposal for Birth than Bodin et al. (2012) due to the different parameterization used here. The other proposals are the same. For the birth step, we added a new interpolation point at depth $c_{k+1}^{'}$, and then assigned a new velocity perturbation value

$v_{k+1}^{'}$ to this new node. This is drawn from a Gaussian proposal probability density:

$$q(v_{k+1}^{'}|v_*) = \frac{1}{\theta_{birth}\sqrt{2\pi}}\exp\left\{-\frac{(v_{k+1}^{'}-v_*)^2}{2\theta_{birth}^2}\right\} \tag{12}$$

where $v_*$ is the current velocity perturbation value at the depth $c_{k+1}^{'}$ where birth takes place. The value of $v_*$ can be calculated by a simple interpolation between its two nearest nodes. The standard deviation $\theta_{birth}$ of the Gaussian distribution is a parameter to be chosen. We refer the reader to Bodin et al. (2012) for the proposal distributions of other types of perturbation.

New models generated from those perturbations are then randomly accepted or rejected according to the acceptance ratio. In order to converge to the target distribution $p(m|\mathbf{d}_{obs})$, the acceptance probability from the current model $\mathbf{m}$ to the proposed model $\mathbf{m}^{'}$, $\alpha(\mathbf{m}^{'}|\mathbf{m})$, has to meet the following requirement:

$$\alpha(\mathbf{m}^{'}|\mathbf{m}) = min\Big[1, \frac{p(\mathbf{m}^{'})}{p(\mathbf{m})}\cdot\frac{p(\mathbf{d}_{obs}|\mathbf{m}^{'})}{p(\mathbf{d}_{obs}|\mathbf{m})}\cdot\frac{q(\mathbf{m}|\mathbf{m}^{'})}{q(\mathbf{m}^{'}|\mathbf{m})}\cdot|\mathbf{J}|\Big], \tag{13}$$

where the matrix $\mathbf{J}$ is the Jacobian of the transformation from $\mathbf{m}$ to $\mathbf{m}^{'}$.

The derivations of acceptance probability in rj-MCMC method were given by Bodin et al. (2012), Appendix C. Here we will only describe the ideas briefly and show the equations that differ from theirs. For moves without change of dimension, both the Jacobian term and the ratio of proposal distributions are 1 and the reader can find the same results as Bodin et al. (2012) by inserting Eqs. 9 and 10 into Eq. 13. For the birth and death steps which involve a change of dimension, it can be shown that the Jacobian term is equal to 1. However, due to the different birth proposal distribution we selected, the expression for the acceptance term for the birth and death steps are different from Bodin et al. (2012). For the birth step:

$$\alpha(\mathbf{m}^{'}|\mathbf{m}) = min\Big[1, \frac{\theta_{birth}\sqrt{2\pi}}{\Delta v}\cdot\exp\left\{\frac{(v_{k+1}^{'}-v_*)^2}{2\theta_{birth}^2}-\frac{M(\mathbf{m}^{'})-M(\mathbf{m})}{2}\right\}\Big], \tag{14}$$

where $M(\mathbf{m})$ is the misfit given by (5) for the current model and $M(\mathbf{m}^{'})$ for the proposed model. Meanings of $v_{k+1}^{'}$ and $v_*$ are the same as in (12). For death step:

$$\alpha(\mathbf{m}^{'}|\mathbf{m}) = min\Big[1, \frac{\Delta v}{\theta_{birth}\sqrt{2\pi}}\cdot\exp\left\{-\frac{(v_j^{'}-v_i^{'})^2}{2\theta_{birth}^2}-\frac{M(\mathbf{m}^{'})-M(\mathbf{m})}{2}\right\}\Big], \tag{15}$$

where $v_i$ is the velocity of the ith interpolation point to be removed at depth $c_i$ and $v_*$ is the velocity at depth $c_i$ in the new structure after the removal of the ith node.

If the newly proposed model is rejected, then the last model is retained for another iteration. The Markov chain is generated via hundreds of thousands of iterations. The first part of the chain (called the burn-in period) is discarded, after which the random walk is assumed to be stationary and starts to sample the model space according to the posterior distribution $p(\mathbf{m}|\mathbf{d}_{obs})$. If the algorithm is run

long enough, these samples should then provide a good approximation of the structure of Earth as constrained by the data.

This ensemble solution contains many models with variable parameterization, and each $V_S$ model in the ensemble corresponds to one dispersion relationship. The expected dispersion is the weighted average through the posterior distribution sampled by the rj-MCMC algorithm. One can use this average to choose one dispersion curve for interpretation purpose.

### 2.4 Forward modeling and Parametrization

In this study, we seek a 1-D depth-dependent isotropic shear velocity model to represent the dispersion of multiple modes between a chosen source and receiver. The isotropic nature of the model is assumed mainly for computational reason, but it is a reasonable assumption as demonstrated by Visser (2008) who showed that the differences in the phase velocities calculated assuming isotropy or anisotropy are small. The $V_S$ profile is described by a variable number $k$ of interpolation points (Figure 2). The vertical position of these points defines the depths at which $V_S$ is perturbed and the horizontal position of these points correspond to the amount $V_S$ is perturbed relative to a reference model using the velocity prior described by Eq. 11.

We adopted the rj-MCMC algorithm (Bodin and Sambridge, 2009) to explore the model space and sample the distribution of model parameters informed by the data. The procedure of our waveform inversion can be summarized as follows:

(1) Choose path-specific reference 1-D shear velocity model
(2) Calculate normal mode eigenfrequencies for the reference model using MINEOS, i.e. solving the fully non-linear equations (Eq. 1)
(3) Generate path-specific 1-D shear velocity model by perturbing the reference model according to the proposal distribution of the rj-MCMC scheme;
(4) Compute the synthetic seismogram predicted by the 1-D model using Eq. 3;
(5) Calculate the misfit between synthetic and observed waveforms (Eq. 5);
(6) Randomly accept or reject the proposed model according to the acceptance ratio;
(7) If the model is accepted, calculate and save the phase velocities predicted by the model using Eq. 4 and generate a new $V_S$ model by perturbing the accepted model according to the proposal distribution. If the model is rejected, generate a new $V_S$ model by perturbing the previously accepted model according to the proposal distribution;
(8) Repeat steps (4) to (7) to generate the Markov chains;
(9) Gather all the saved phase velocities to determine the distribution of dispersion curves obtained at each period/frequency;

(10) Calculate the mean and standard deviation of these distributions to obtain a measured dispersion curve and phase velocities uncertainties, respectively;

(11) Estimate the reliability of the dispersion curves (see section 2.5).

### 2.5 Reliability Analysis

In principle, with the proposed method we are able to obtain the phase velocities for any mode at any period since they are calculated from the ensemble of $V_S$ models obtained. However, in practice, only some modes at certain periods can be reliably constrained by a single seismogram. It is thus important to estimate the reliability of the measurements in each frequency band for different modes. Here, we adopted a procedure similar to Yoshizawa and Kennett (2002) based on the Frequency Time Analysis method (Dziewonski et al., 1969).

Let us first define the waveform fit $f(\omega, t)$:

$$f(\omega, t) = \exp\left[-\frac{S^{\text{mis}}(\omega, t)}{S^{\text{syn}}(\omega, t)}\right] \tag{16}$$

where $S^{\text{mis}}(\omega, t)$ represents the spectrogram of the difference between real data and the inverted synthetics. $S^{\text{syn}}(\omega, t)$ is the spectrogram of the whole synthetic waveform. Similarly, the relative power of the $j$th mode $p_j(\omega, t)$ is defined as:

$$p_j(\omega, t) = \exp\left[-\frac{S_j^{\text{res}}(\omega, t)}{S_j^{\text{syn}}(\omega, t)}\right] \tag{17}$$

where $S_j^{\text{syn}}(\omega, t)$ is the spectrogram of the $j$th mode waveform, and $S_j^{\text{syn}}(\omega, t)$ is the spectrogram of the residual seimogram calculated as the difference between the full synthetic and the $j$th mode waveform. In practice, both the frequency $\omega$ and time $t$ are discrete, so the spectrograms can be expressed in matrix form. For example, the element in the $k$th row and $l$th column of the spectrogram matrix represents the amplitude of $S(\omega_k, t_l)$, where $\omega_k$ is the discretized frequency and $t_l$ is the center of the $l$th time window used in the frequency-time (F-T) domain analysis.

The waveform fit $\mathbf{f}$ measures the difference between the synthetic and real data in the F-T domain. It is designed such that $\mathbf{f} = 1$ when the synthetic seismograms are identical to the observed data, and $\mathbf{f}$ decreases when the waveform fit becomes worse. The relative power $\mathbf{p}_j$, which measures the relative power of the $j$th mode, is designed in a similar way so that $\mathbf{p}_j = 1$ when the $j$th mode in the seismogram is completely dominant and there is no contribution from other modes, and $\mathbf{p}_j$ decreases as the contribution from the $j$th mode becomes smaller.

For the reliability analysis, we want to consider the overall waveform fit and the relative weight of one single mode at the same time because both factors indicate how well the phase velocities at certain frequencies are constrained by the data. That is, the measurement of the $j$th mode becomes

more reliable if the waveform fit is better, or if the relative weight of the $j$th mode increases. Following this criteria, we define the reliability parameter as:

$$r_j(\omega) = \sum_l p_j^{kl} f^{kl} \tag{18}$$

where $p$ and $f$ are defined in Eqs. 16 and 17. To get the reliability parameter of the $j$th mode $r_j(\omega)$, we first multiply the waveform fit by the relative weight of the $j$th mode in the F-T domain, and then integrate the resulting matrix with respect to time. In this way, the $r_j(\omega)$ is a function of frequency and can be regarded as an indicator of reliability at frequency $\omega$ for the $j$th mode. Examples of the reliability analysis are shown in section 3.

## 3 TESTS AND RESULTS

### 3.1 Synthetic test

We first present a synthetic test to demonstrate that our method can recover an input shear-wave velocity model well. A shear-wave velocity profile generated by perturbing the Preliminary Reference Earth Model (PREM) (Dziewonski and Anderson, 1981) was used to calculate a synthetic seismogram. Figure 3(B) displays the perturbation $dV_S(r)/V_S(r)$. It is characterized by +3% anomaly relative to PREM at 200km depth and -2% at 600km depth. The synthetic seismogram (Figure 4), representing the velocity of the ground motion, was calculated for a great circle path between the Banda Sea and Beijing, which corresponds to a distance of 5,347km. The event source parameters were taken from the GCMT catalog (Dziewonski et al., 1981; Ekström et al., 2012) and are shown in Table 2. Only the vertical component is considered for the waveform fitting. Uncorrelated Gaussian noise was added to the synthetic data in order to test the robustness of our method. The noise level was set at 10% of the average amplitude of higher mode waveform in the time window defined in Table 1.

The inversion of the synthetic waveform data was performed using 16 Markov chains starting from different random models, with the length of each chain fixed at 120,000 iterations. To guarantee the convergence of the inversion when sampling the posterior distribution, the first 60,000 iterations in each chain were marked as 'burn-in' and we removed them from the ensemble of sampled models. The ensemble of $dV_S/V_S$ solutions represented by a color density plot is displayed in Figure 3(A). The brighter color means the algorithm spent more time in that region, and therefore it corresponds to a more likely $V_S$ structure at that particular depth. The mean output model calculated from the ensemble of solutions (Figure 3(B)), which can be regarded as the expectation of the "true model", is close to the input model. Figure 3(C) displays the posterior distribution of the number of parameters used by the algorithm during the inversion and demonstrates the parsimony of the transdismensional

framework: although we can almost always fit the data better by introducing more parameters, the rj-MCMC method tends to prevent overfitting the data and prefer models of smaller dimensions.

A comparison between the input and output seismograms is shown in Figure 4, which shows that the predicted waveform resulting from our inversion fits the input data much better than the waveform predicted by PREM. The misfit between the inverted waveform and the input data is represented in Figure 5 both in the time domain and the F-T domain.

The fundamental mode and first overtone phase velocity dispersion was calculated and compared with the dispersion relationship predicted by the true model (Figure 6). The standard deviation of our measurements at each period were calculated from the ensemble of dispersion curves obtained. We see that the true dispersion curve is within the 68% likelihood contour of our inversion results at all periods.

We further applied the reliability analysis described in the previous section to our synthetic test. The relative weight of the first overtone is used as an example to demonstrate the method (Figure 7). The spectrogram of misfit in Figure 5 and the spectrograms of relative weights (like in Figure 7) were multiplied using Eq. 18 and summed along the time domain to obtain the reliability parameters as a function of frequency for each mode (Figure 8). In order to automate the process, we arbitrarily define the threshold values at 10 for the fundamental mode and 2 for higher modes. For each mode, only periods with reliability parameters larger than the threshold will be kept. As is shown in the synthetic test results, the fundamental mode and the first overtone have high reliability at all periods. The second overtone is also above the threshold at most periods but the third and fourth higher modes only have a short range of reliable results. The fifth overtone cannot be resolved well in the synthetic test.

### 3.2 Application to real data

In this section we present the phase velocity inversion results for two paths across western and eastern Australia. Figure 9 shows the map of events and stations distribution. The two yellow curves represent the great circle paths from sources to stations NWAO and TAU, which go through Western and Eastern Australia, respectively.

The two events we selected both have depths larger than 50km, which helps detect higher modes. The source parameters of both events are listed in Table 2. The epicentral distance for the western path is 4,036 km, and for the eastern path is 4,012 km. Although a non-linear inversion method is used here to calculate phase velocities from the velocity models, it can still be preferable to use a reference model that is as close as possible to the true structure of the region studied. This is mainly because our method to calculate the synthetic seismograms is not fully non-linear for computational reasons (see section 2). The forward modeling part of the algorithm was linearized, and we search for

model parameters $dV_S/V_S$ between -5% and 5% around a reference model in order to reduce errors caused by the linearization. Here, we adopted the 3-D shear-velocity model of Debayle et al. (2016). We averaged the $V_S$ profiles extracted from the reference model along each each station-event pair, and used this average as a reference model for the specific 1-D path considered.

The posterior distribution of $dV_S/V_S$ models for the western path is shown in Figure 10, followed by the waveform fitting (Figure 11), the reliability analysis (Figure 12), and the estimated phase velocity dispersion curves (Figure 13). The inverted $dV_S/V_S$ structure displays a modest positive deviation from the reference model at 100km depth, but little perturbation at greater depths. Overall, our inversion results give a path-averaged $V_S$ that is consistent with what is expected for a path sampling mostly a craton, with a 250km thick high velocity zone in the uppermost mantle, which may be interpreted as the seismic lithosphere. Since most published papers present velocity anomalies with respect to 1-D velocity models instead of a 3-D model such as the one used here, we also provided a plot of $dV_S/V_S$ with respect to PREM for completeness (Figure 14(A)).

The synthetic waveform calculated from the mean velocity model fits the real data well (Figure 11), and we see that phase velocities for the fundamental mode has reliability parameters larger than the predefined threshold, 10, at all periods considered (Figure 12). For the first overtone, the reliable measurements are in the period range $92-200s$, with the threshold set at 2. Similarly, the second overtone phase velocities were estimated to be reliable in the period range $88-150s$. The reliability parameters of the third overtones consist of 2 part: $60-66s$ and $75-86s$. Finally, a small portion ($50-59s$) of the fourth overtone was found to be reliable.

For the eastern Australia path, we repeated the procedure described above. The results are shown in Figs. 15-18. We see a strong positive $V_S$ anomaly compared to the reference model at about 60km depth and a negative $V_S$ anomaly at $120-220km$ depth. Our solution can be interpreted as a thin lithosphere (about 100km thick) with slightly positive velocity anomalies and a low velocity layer that may coincide with the asthenosphere (Fig. 14(B)), consistent with Phanerozoic geological features and with previous studies (Yoshizawa and Kennett, 2015). It should also be noted, however, that our $V_S$ solutions are not directly comparable with 3-D models, but rather can be regarded as a 1-D approximation of the real Earth structure along the selected path. With Figure 17, we show that the fundamental mode and the first four overtones can be reliably retrieved: the fundamental mode has high reliability at most periods considered. The first and second overtones have large reliability at higher periods ($60-200s$, $54-62s$ and $68-200s$). The reliable periods for third and fourth overtones are $50-88s$ and $50-62s$, respectively. Measurements for the modes and periods estimated reliable are shown in Fig. 18. This figure also displays phase velocities measured using S40RTS (Ritsema et al., 2011) as a reference instead of the Debayle et al. (2016) model to test the dependence of our method upon the

reference model. The results show no significant dependence on the reference model. The reliability tests were not strongly affected by the reference model either (not shown here).

In this study we used the centroid moment tensor from the GCMT catalog. We acknowledge, however, that for some paths dispersion measurements performed using waveform modeling at single stations can be affected by uncertainties in source parameters. While quality control can be applied to filter out unreliable earthquake sources by comparing source parameters from different earthquakes in the same region or by comparing different source catalogues, joint inversions of structure and source parameters are preferable (Valentine and Trampert, 2012). A future implementation of our technique will include source parameter among the unknowns in order account for possible errors in the source parameters.

## 4 CONCLUSION

We applied a rj-MCMC technique to the non-linear problem of measuring fundamental and higher mode Rayleigh wave phase velocity dispersion using waveform modeling. The use of higher mode surface waves in depth inversions of seismic velocities and anisotropy is very valuable as it increases the vertical resolution of tomographic models in the upper mantle and transition zone. The forward problem consisted in calculating synthetic seismograms by normal mode summation using computer program Mineos and a linearized approximation to the calculation of normal mode eigenfrequencies. The rj-MCMC method enabled us to find a distribution of 1-D shear velocity models that best fit the waveform and represent the dispersion of multiple modes along a specific source-receiver path. The resulting distribution of velocity models was used to calculate a posterior distribution of dispersion curves, from which a mean and standard deviation were obtained for different modes. A reliability analysis was then performed following Yoshizawa et al. (2002) to assess which higher modes were reliably separated.

With synthetic tests, we showed that the newly developed method presented here can separarate the first four overtones and the fundamental mode at most perios between 50 and 200s, but that the third and fourth overtones can only be measured reliably at relatively short periods and in a narrower period band (50-100s for n=3 and 50-60s for n=4). Measurements performed for real data along two paths sampling western and eastern Australia showed similar results: the fundamental mode and first two overtones were measured reliably over most frequencies considered, and the third and fourth overtones could be separated and their dispersion measured over a narrower frequency band and for shorter periods. We also demonstrated that the measured phase velocities do not strongly depend on the reference model used to calculate the initial seismogram.

While computationally intensive, the technique presented here has several advantages. It allows

the user to sample the model space without requiring any explicit regularization other than specifying the bounds of the model space explored. In addition, because it is transdismensional and parsimonious, it can include data noise and the number of parameters among the unknowns without overfitting the data. It therefore lets the data themselves control the complexity of the solution. The reliability of mode separation can be assessed and quantitative uncertainties on the dispersion curves of each mode can be readily obtained. This provides useful information on the data to seismologists who use these measurements to model three-dimensional seismicvelocity and anisotropy. Our technique can also be easily adapted to include source parameters among the unknowns and perform joint inversions of model structure and source parameters to account for the effect of source uncertainties on the measured phase velocities.

## ACKNOWLEDGMENTS

We wish to thank Thomas Bodin for sharing his original MCMC code. The code was modified by H.X. to incorporate program MINEOS, which is freely available on the CIG website at `http://www.geodynamics.org/`. Calculations were made on C.B.'s computer cluster, which was funded by NSF grant #0949255. Figures were made using Matlab and the Python plotting library Matplotlib (Hunter, 2007).

## REFERENCES

Backus, G. E. (1988), Bayesian inference in geomagnetism, *Geophysical Journal*, **92** 125-142. doi:10.1111/j.1365-246X.1988.tb01127.x

Bayes, T. (1763), An essay towards solving a problem in the doctrine of chances, *Philos. Trans. R. Soc. London*, **53**, 370-418. [Reprinted in Biometrika, 45, 295-315, 1958.]

Beucler, E., Stutzmann, E. and Montagner, J. P. (2003), Surface wave higher-mode phase velocity measurements using a roller-coaster-type algorithm, *Geophys. J Int.*, **155**(1), 289-307.

Bodin, T., and M. Sambridge (2009), Seismic tomography with the reversible jump algorithm, *Geophys. J Int.*, **178**(3), 1411-1436.

Bodin, T., M. Sambridge, H. Tkalčić, P. Arroucau, K. Gallagher, and N. Rawlinson (2012), Transdimensional inversion of receiver functions and surface wave dispersion, *J. geophys. Res.*, **117**, B02301, doi:10.1029/2011JB008560.

Cara, M. (1973), Filtering of dispersed wavetrains, *Geophys J Roy Astron Soc.*, **33**(1), 65-80.

Cara, M. (1978), Regional variations of higher Rayleigh-mode phase velocities: A spatial-filtering method, *Geophys. J Int.*, **54**(2), 439-460.

Cara, M. (1979), Lateral variations of S velocity in the upper mantle from higher Rayleigh modes, *Geophys. J Int.*, **57**(3), 649-670.

Cara, M. and Lévêque, J. J. (1987), Waveform inversion using secondary observables, *Geophys. Res. Lett.*, **14**(10), 1046-1049.

Crampin, S. (1964), Higher Modes of Seismic Surface Waves: Preliminary Observations, *Geophys. J Int.*, **9**(1), 37-57, doi:10.1111/j.1365-246X.1964.tb06313.x

Dahlen, F. A. and Tromp, J. (1998), Theoretical global seismology, *Princeton University Press*, Princeton.

Debayle, E. (1999), SV-wave azimuthal anisotropy in the Australian upper mantle: preliminary results from automated Rayleigh waveform inversion, *Geophys. J Int.*, **137**, 747-754, doi:10.1046/j.1365-246x.1999.00832.x

Debayle, E., Dubuffet, F., and Durand, S. (2016), An automatically updated S-wave model of the upper mantle and the depth extent of azimuthal anisotropy, *Geophys. Res. Lett.*, **43**, 674-682, doi:10.1002/2015GL067329.

Dziewonski, A., Bloch, A., and Landisman, M. (1964), A Technique for the Analysis of Transient Seismic Signals, *Bull. seism. Soc. Am.*, **59**(1), 427-444.

Dziewonski, A. and Anderson, D.M. (1981), Preliminary reference Earth model, *Phys. Earth Planet. Inter.*, **25**(4), 297-356.

Dziewonski, A. M., T.-A. Chou and J. H. Woodhouse (1981), Determination of earthquake source parameters from waveform data for studies of global and regional seismicity, *J. geophys. Res.*, **86**, 2825-2852. doi:10.1029/JB086iB04p02825

Ekström, G., M. Nettles, and A. M. Dziewonski (2012), The global CMT project 2004-2010: Centroid-moment tensors for 13,017 earthquakes, *Phys. Earth Planet. Inter.*, **200-201**, 1-9, doi:10.1016/j.pepi.2012.04.002

Geyer, C., and J. Møller (1994), Simulation procedures and likelihood inference for spatial point processes, *Scand. J. Stat.*, **21**(4), 359-373.

Hunter, J. D. (2007), Matplotlib: A 2D graphics environment, *Computing in science & engineering*, **9**(3), 90-95.

Jeans, J. H. (1923), The Propagation of Earthquake Waves, *Proc. R. Soc. Lond. Series A, Containing Papers of a Mathematical and Physical Character*, **102**(718), 554-574, doi:10.1098/rspa.1923.0015

Laske, G. and Widmer-Schnidrig, R. (2015), Normal Mode & Surface Wave Observations, in *Treatise on Geophysics: Seismology and Structure of the Earth*, Vol. 1 (2nd edition), 117-165.

Lebedev, S. and Nolet, G. (2003), Upper mantle beneath Southeast Asia from S velocity tomography, *J. geophys. Res.*, **108**(B1), doi:10.1029/2000JB000073.

Lerner-Lam, A. L. and Jordan, T. H. (1983), Earth structure from fundamental and higher-mode waveform analysis, *Geophys. J Int.*, **75**(3), 759-797.

Lévêque, J. J., Cara, M. and Rouland, D. (1991), Waveform inversion of surface wave data: test of a new tool for systematic investigation of upper mantle structures, *Geophys. J Int.*, **104**(3), 565-581.

Li, X. and Romanowicz, B. (1995), Comparison of global waveform inversions with and without considering cross-branch modal coupling, *Geophys. J Int.*, **121**, 695-709.

Li, X. and Romanowicz, B., (1996), Global mantle shear velocity model developed using nonlinear asymptotic coupling theory, *J. geophys. Res.*, **101**,22 245-22 273.

Maggie, A., Debayle, E., Priestley, K., and Barruol, G. (2006), Azimuthal anisotropy of the Pacific region, *Earth Planet. Sci. Lett.*, **250**, 53-71, doi:10.1016/j.epsl.2006.07.010

Malinverno, A. (2002), Parsimonious Bayesian Markov chain Monte Carlo inversion in a nonlinear geophysical problem, *Geophys. J Int.*, **151**(3), 675-688

Masters, G., Woodhouse, J.H., Freeman, G. (2011), Mineos v1.0.2 [software], *Computational Infrastructure for Geodynamics*, `https://geodynamics.org/cig/software/mineos/`

Montagner, J.-P. (1986), Regional There-dimensional structures using long-period surface waves, *Annales Geophysicae*, **4**(B3), 283-294

Nolet, G. (1975), Higher Rayleigh modes in western Europe, *Geophys. Res. Lett.*, **2**(2), 60-62, doi:10.1029/GL002i002p00060

Nolet, G. (1990), Partitioned waveform inversion and two-dimensional structure under the network of autonomously recording seismographs, *J. geophys. Res.*, **95**(B6), 8499-8512, doi:10.1029/JB095iB06p08499

Ritsema, J., Deuss, A., van Heijst, H.J., and Woodhouse, J.H. (2011), S40RTS: a degree-40 shear-velocity model for the mantle from new Rayleigh wave dispersion, teleseismic traveltime and normal-mode splitting function measurements, *Geophys. J Int.*, **184**(3), 1223-1236, doi:10.1111/j.1365-246X.2010.04884.x

Roult, G. and Romanowicz, B. (1984), Very long-period data from the GEOSCOPE network: Preliminary results on great circle averages of fundamental and higher Rayleigh and Love modes, *Bull. seism. Soc. Am.*, **74**(6), 2221-2243

Sambridge, M. (1999a), Geophysical inversion with a Neighbourhood Algorithm -I. Searching a parameter space, *Geophys. J Int.*, **138**, 479-494.

Sambridge, M. (1999b), Geophysical inversion with a Neighbourhood Algorithm -II. Appraising the ensemble, *Geophys. J Int.*, **138**, 727-746.

Stutzmann, E. and Montagner, J. P. (1993), An inverse technique for retrieving higher mode phase velocity and mantle structure, *Geophys. J Int.*, **113**, 669-683.

Montagner, J. P., Romanowicz, B. and Karczewski, J. F. (1994), A first step toward an oceanic geophysical observatory, *Eos, Transactions American Geophysical Union*, **75**(13), 150-154.

Valentine, A.P. and Trampert, J. (2012), Assessing the uncertainties on seismic source parameters: Towards realistic error estimates for centroid-moment-tensor determinations, *Phys. Earth Planet. Inter.*, **210-211**, 36-49, doi:10.1016/j.pepi.2012.08.003.

van Heijst, H.J. and Woodhouse, J.H. (1997), Measuring surface-wave overtone phase velocities using a mode-branch stripping technique, *Geophys. J Int.*, **131**, 209-220.

Visser, K., Lebedev, S., Trampert, J. and Kennett, B.L.N (2007), Global Love wave overtone measurements, *Geophys. Res. Lett.*, **34**, L03302, doi:10.1029/2006GL028671.

Visser, K., (2008), Monte Carlo search techniques applied to the measurements of higher mode phase velocities and anisotropic surface wave tomography, *PhD thesis*, Utrecht University, the Netherlands.

Woodhouse, J.H. (1980), The coupling and attenuation of nearly resonant multipiers in the Earth's free oscillation spectrum, *Geophys. J. R. Astr. Soc.*, **61**, 261-283.

Yoshizawa,K. and Kennett, B.L.N. (2002), Non-linear waveform inversion for surface waves with a neighbourhood algorithm: application to multimode dispersion measurements, *Geophys. J Int.*, **149**, 118-133.

Yoshizawa,K. and Kennett, B.L.N. (2004), Multi-mode surface wave tomography for the Australian region using a three-stage approach incorporating finite frequency effects, *J. geophys. Res.*, **109**, B02310, doi:10.1029/2002JB002254.

Yoshizawa,K. and Kennett, B.L.N. (2015), The lithosphere-asthenosphere transition and radial anisotropy beneath the Australian continent, *Geophys. Res. Lett.*, **42**, 3839-3846, doi:10.1002/2015GL063845.

**Table 1.** Selection of frequency-time windows

| **frequency(mHz)** | **Group velocity (km/s)** |
|---|---|
| 5-10 | $3.7 \pm 0.75$ |
| 10-20 | $3.75 \pm 0.55$ |
| | b-4.3 |

**Table 2.** Source parameters from GCMT Catalog. The event 200503021042A is used for the synthetic test. 200910151211A for the west Australia path and 201004172315A for the east Australia path.

| **ID** | **date** | **time** | **lat(°)** | **lon(°)** | **depths(km)** | $M_0$**(dyne-cm)** | **strike,dip,rake** |
|---|---|---|---|---|---|---|---|
| 200503021042A | 2005/03/02 | 10:42:16.9 | -6.54 | 129.99 | 196.1 | 5.73e+26 | 41,88,55 |
| 200910151211A | 2009/10/15 | 12:11:19.8 | -3.04 | 139.45 | 105.1 | 1.34e+25 | 296,83,145 |
| 201004172315A | 2010/04/17 | 23:15:27.9 | -6.82 | 147.30 | 62.9 | 2.19e+25 | 268,50,91 |

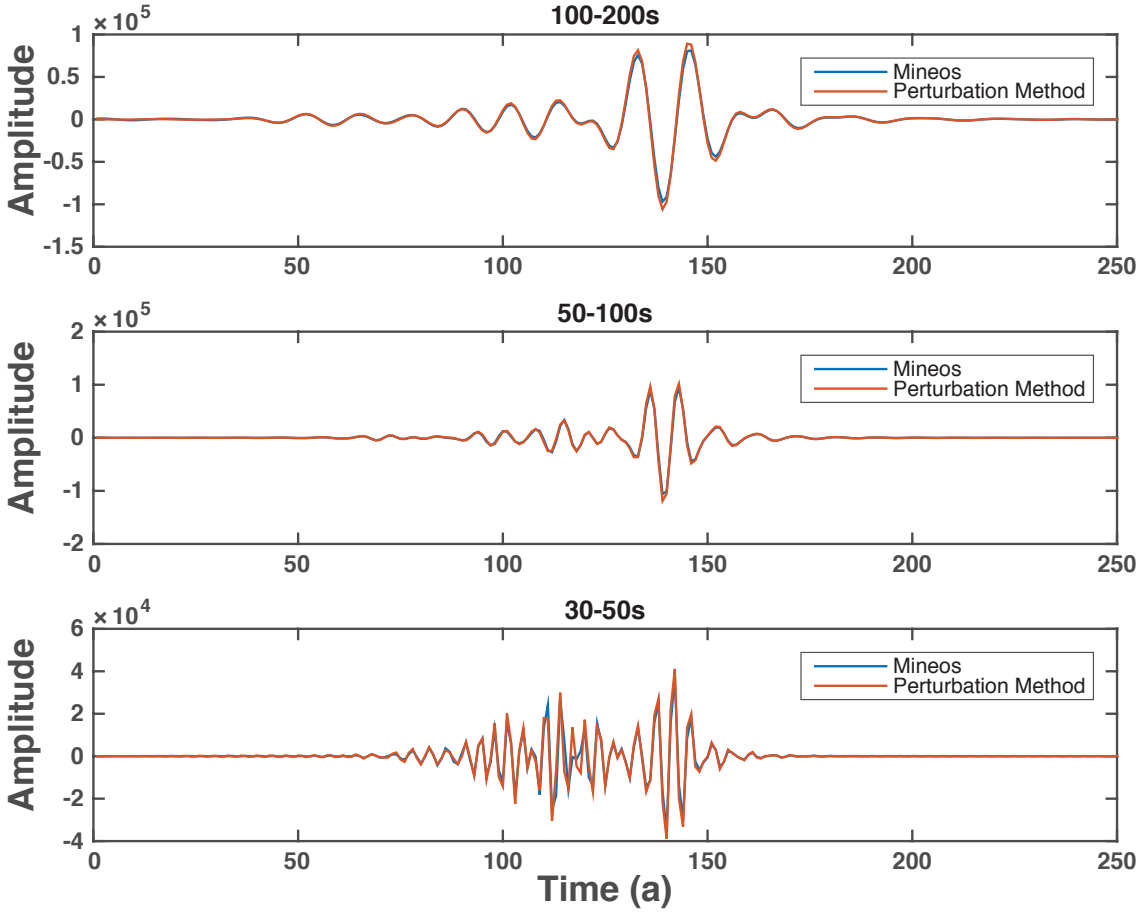


**Figure 1.** Comparison between synthetic seismograms calculated with fully non-linear Mineos (blue) and with our linearized method (red) in three different period ranges: 100-200 s (top), 50-100 s (middle), and 30-50 s (bottom). The shear-velocity model used to compute the seismograms is shown in Figure 2.

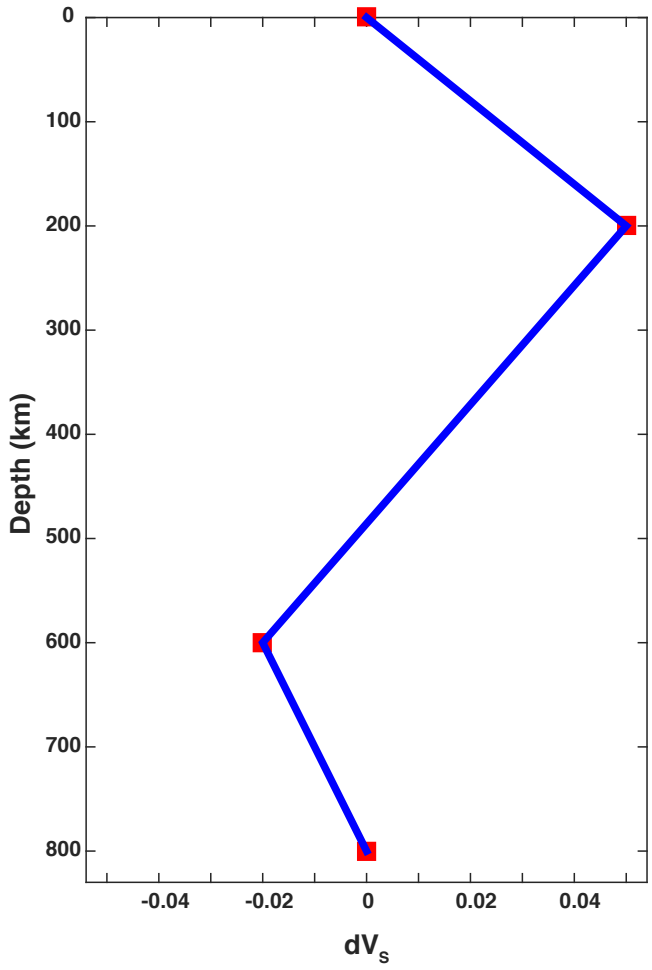


**Figure 2.** Example of model parametrization. The red squares denote the points at which the velocity model is perturbed. The complete $dV_S$ profile is obtained by linear interpolation between those points.

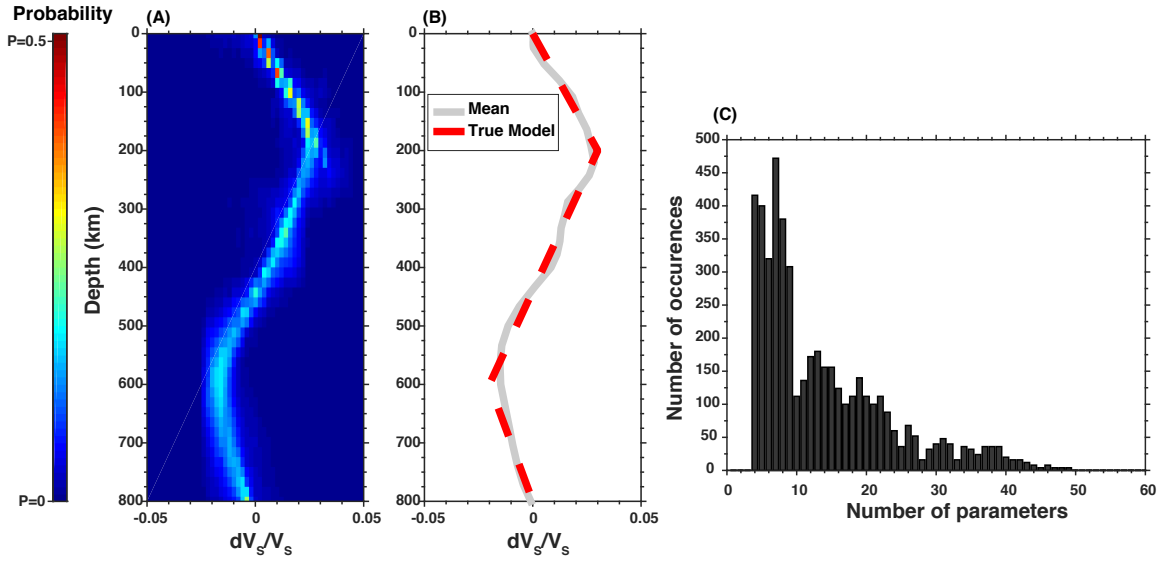


**Figure 3.** (A) Color density plot representing the ensemble of solutions obtained by inversion of the synthetic seismogram that was calculated with the input model shown in (B). The posterior mean model resulting from this distribution of solutions is also displayed in (B); (C) Posterior distribution for the number of parameters.

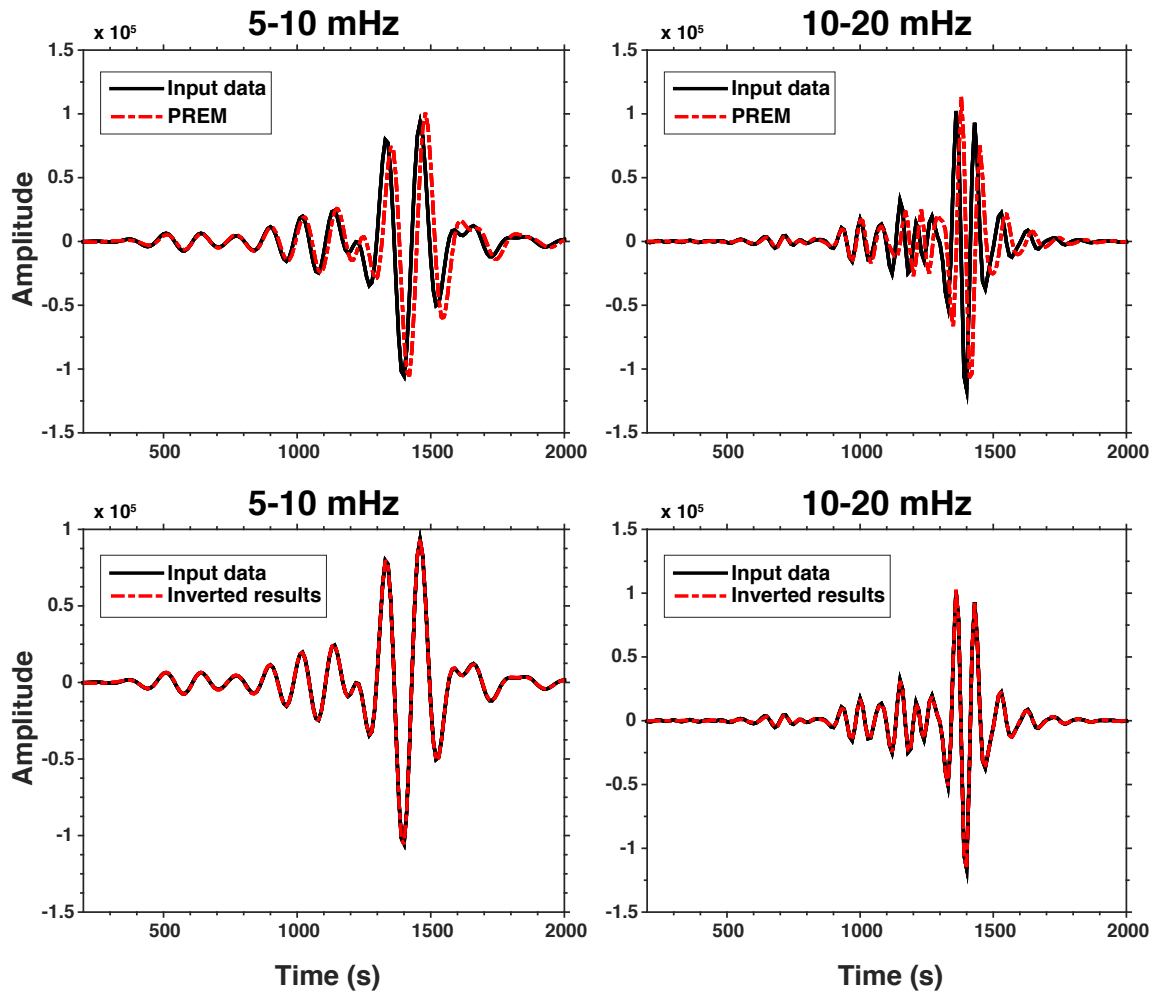


**Figure 4.** Comparison between input synthetic waveform and the waveform predicted by PREM (top) and by the mean model resulting from our inversion (bottom). The seismograms shown here represent the velocity of the ground motion. The input seismogram was calculated for the true model shown in Figure 3. Two frequency bands, as indicated in table 1, are considered separately. The waveforms match is much improved after inversion.

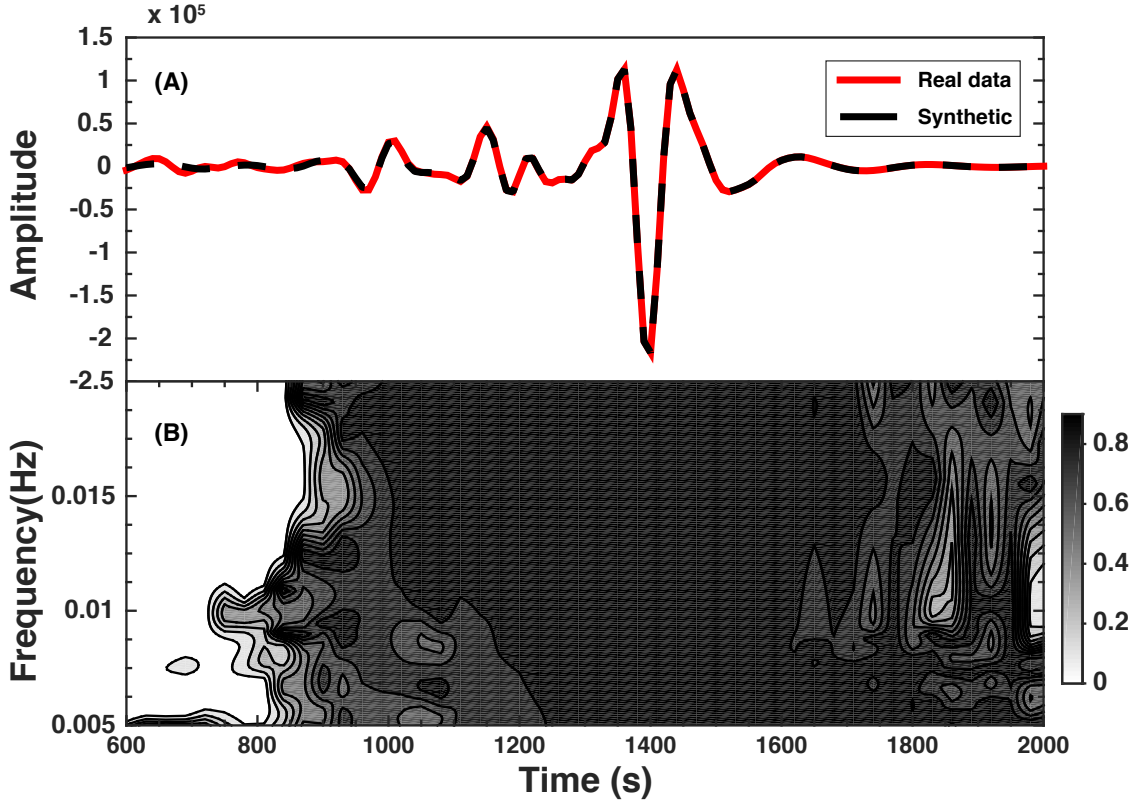


**Figure 5.** (A) Comparison between the output and input synthetic data in the time domain; (B): Spectrogram of the waveform fit $f(\omega, t)$, as defined in equation 16. The darker regions correspond to better waveform fit in the F-T domain.

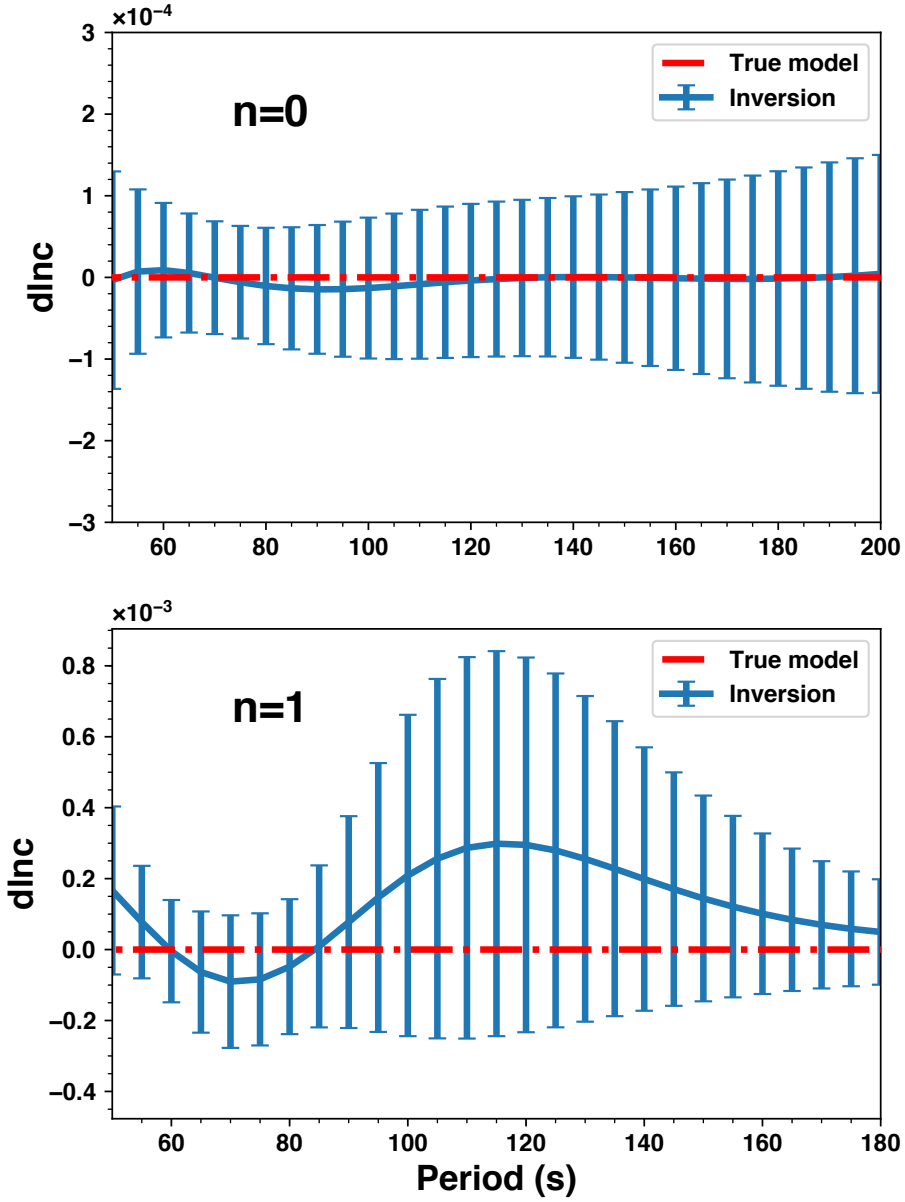


**Figure 6.** Inverted fundamental mode (top) and first overtone (bottom) phase velocity dispersion and uncertainties (blue) compared to the dispersion curve calculated for the true model (red). The uncertainties shown here correspond to $1\sigma$ obtained from the posterior distribution.

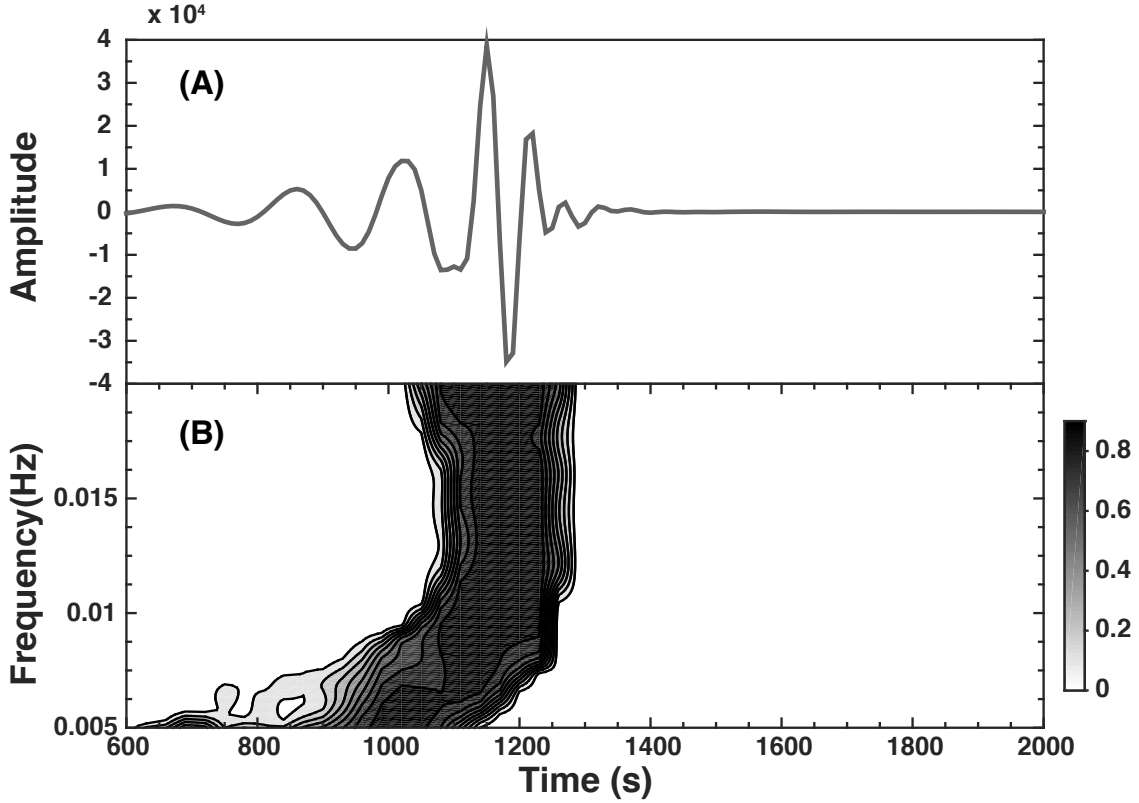


**Figure 7.** (A) Synthetic waveform of the first overtone calculated from the inverted 1-D $Vs$ profile; (B): Spectrogram $\mathrm{P}_1(\omega, t)$ of the relative weight of the first overtone in the synthetic test, as defined in equation 17. The darker regions in the figure represent larger weights in the F-T domain.

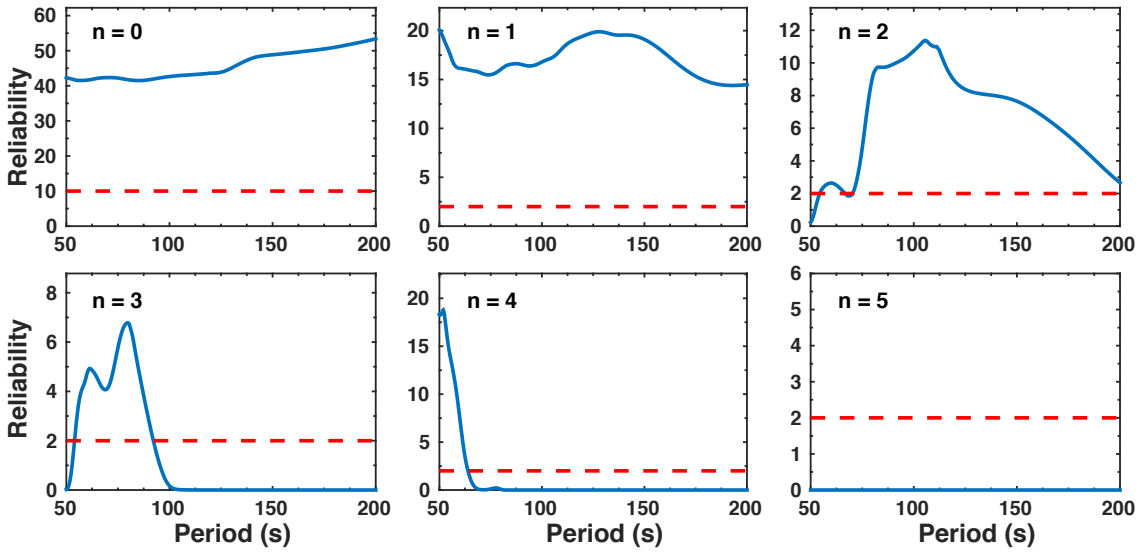


**Figure 8.** Reliability parameters as a function of frequency for the fundamental mode (n=0) and the first five overtones in the synthetic test. The thresholds we defined for each mode are denoted by the red dashed lines. Only periods at which the reliability parameters are above the threshold are kept as reliable inversion results.

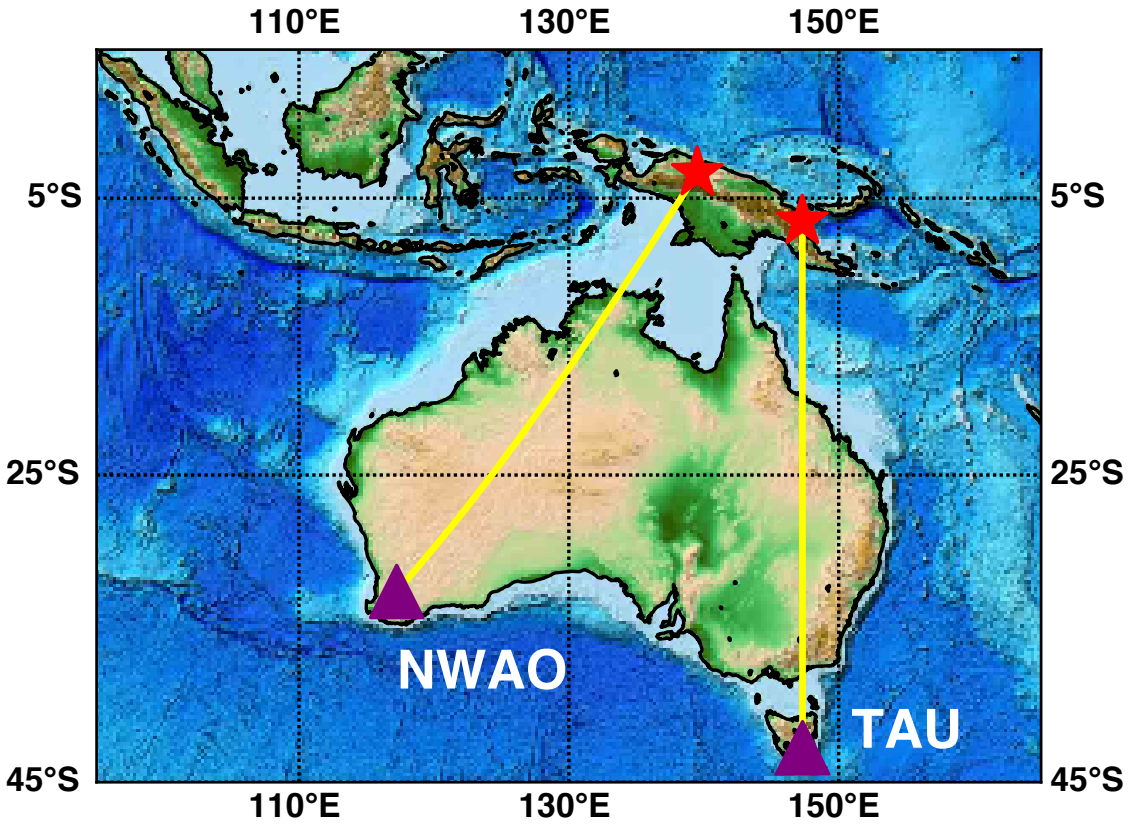


**Figure 9.** Locations of events (red stars) and stations (purple triangles) used for the real data test. The yellow lines show the great circle paths from sources to receivers.

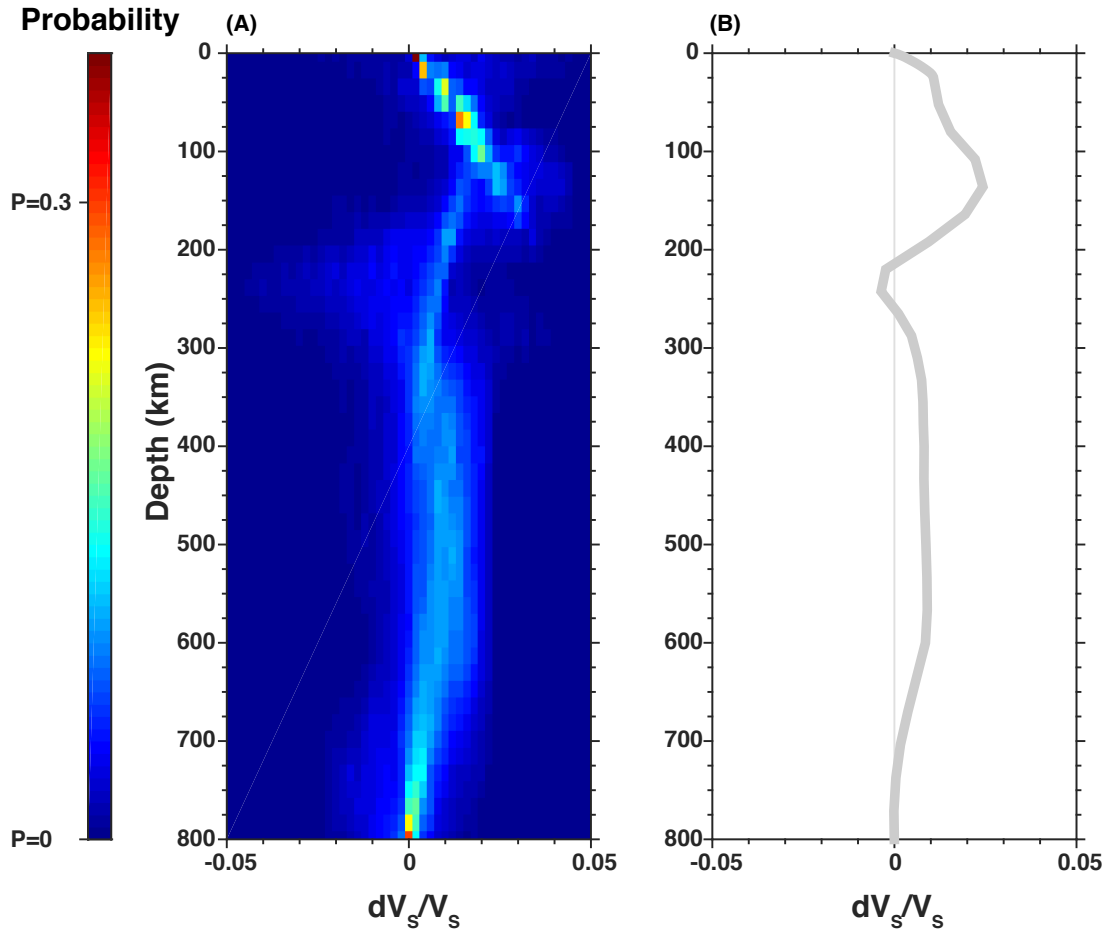


**Figure 10.** Posterior distribution of relative velocity perturbations with respect to the model of Debayle et al.(2016) (A) and resulting mean $dV_S/V_S$ model (B) obtained for the western Australia path.

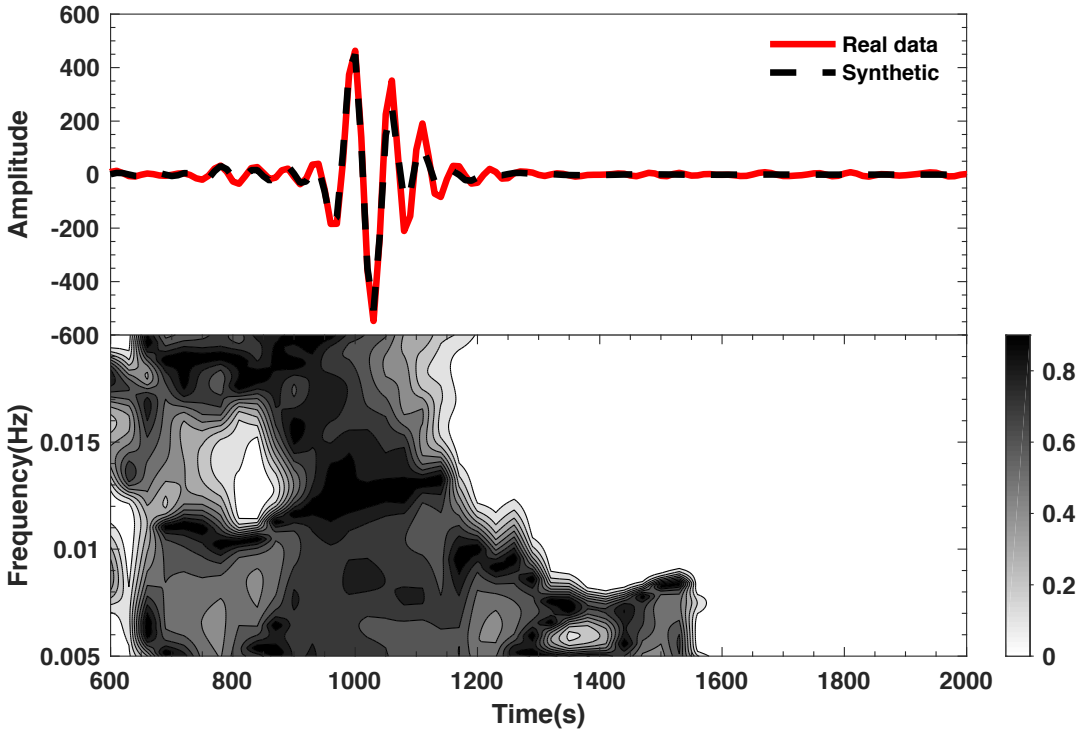


**Figure 11.** The same as Figure 5 but for the western Australia path. (A): real data and synthetic seismogram calculated using the inverted mean model of Figure 10; (B) F-T analysis of the misfit as defined in equation 16.

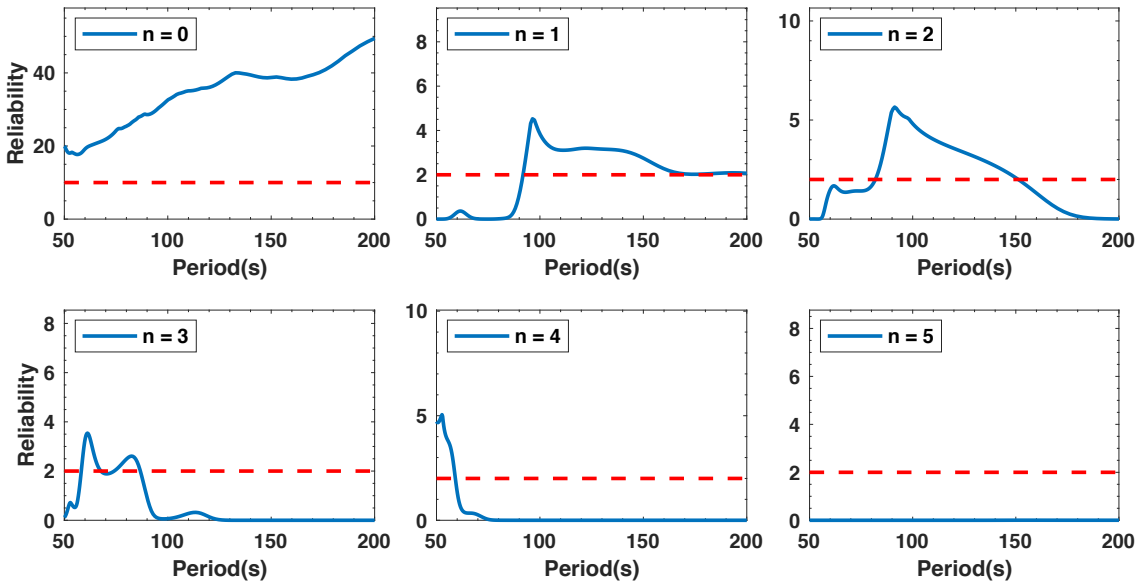


**Figure 12.** Reliability parameters for the western Australia path. See Figure 8 for details.

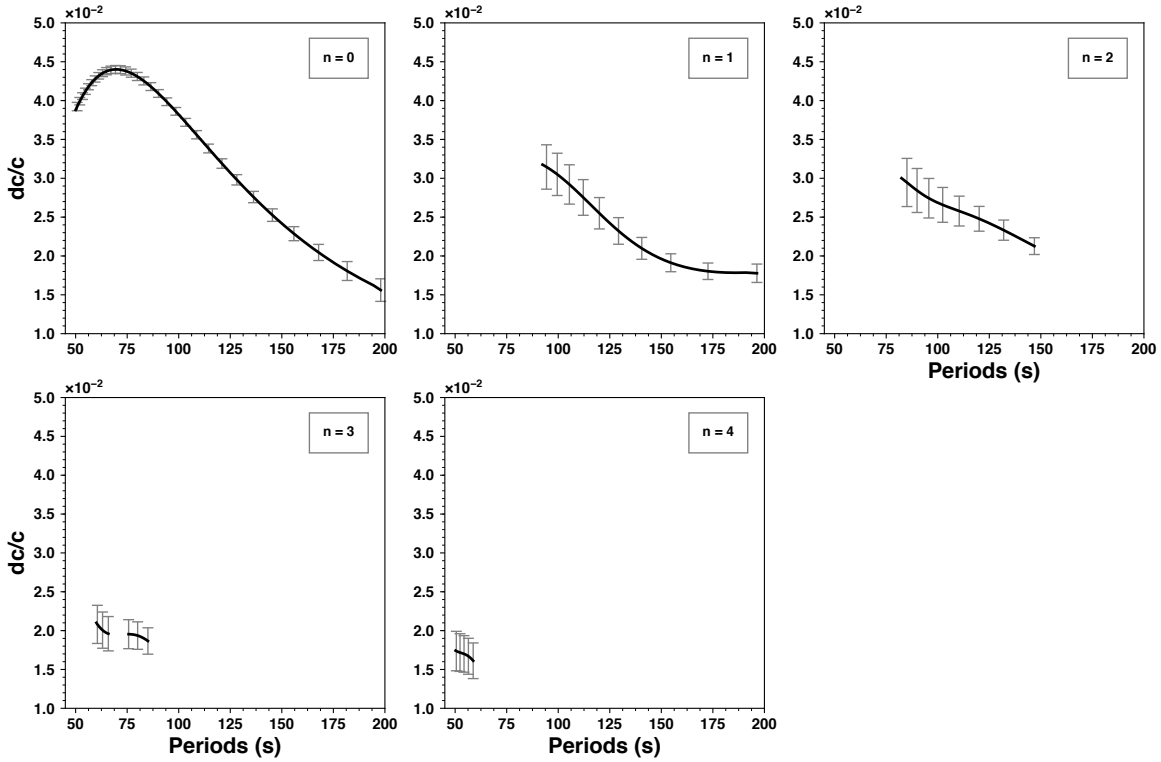


**Figure 13.** Measured phase velocities anomalies for the western Australia path and the modes and periods that were estimated to be reliable (Fig. 12). The measurements were converted from perturbations with respect to the 3-D reference model into perturbations with respect to PREM. Uncertainties correspond to $1\sigma$.

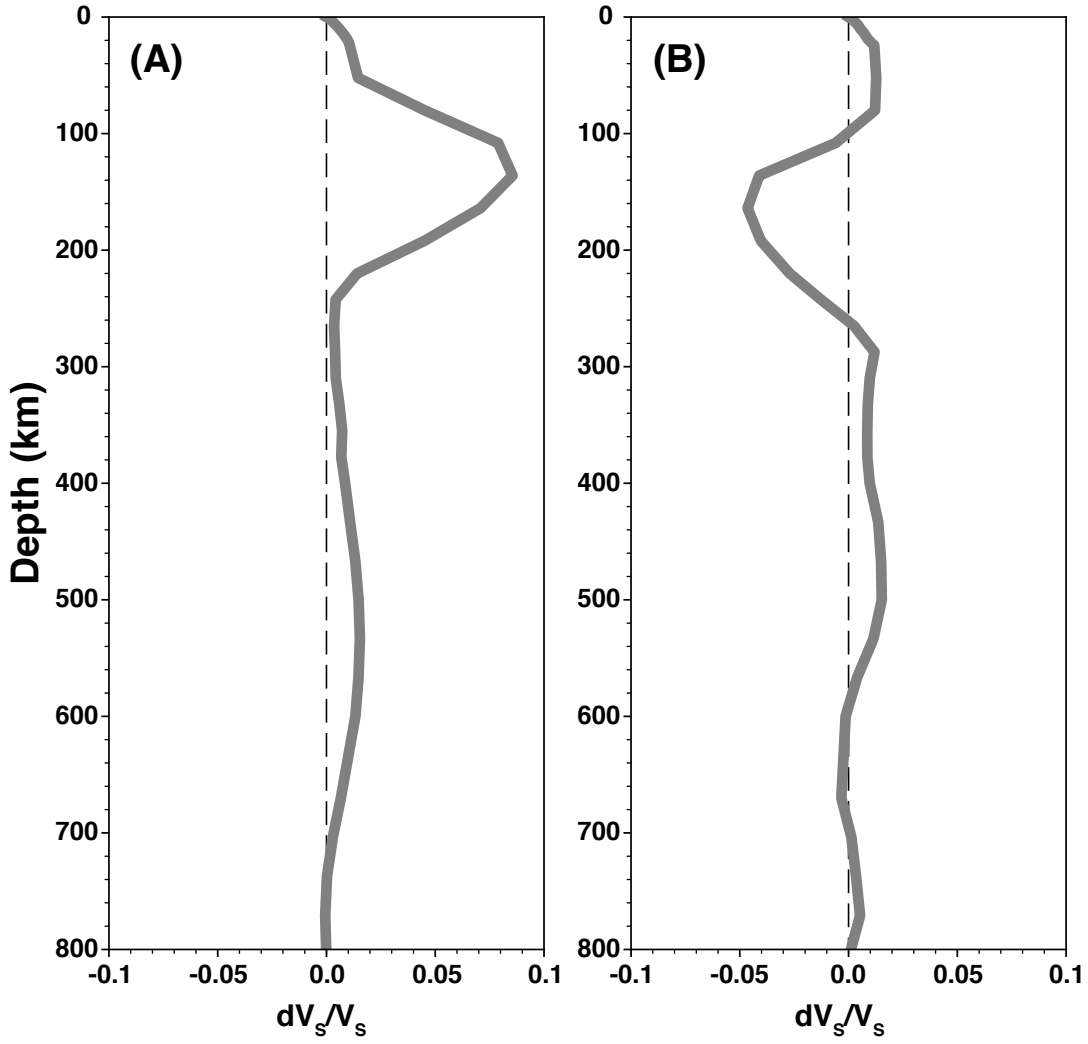


**Figure 14.** The mean $dV_S/V_S$ solution for the western (A) and Eastern (B) Australia paths plotted as perturbations with respect to PREM.

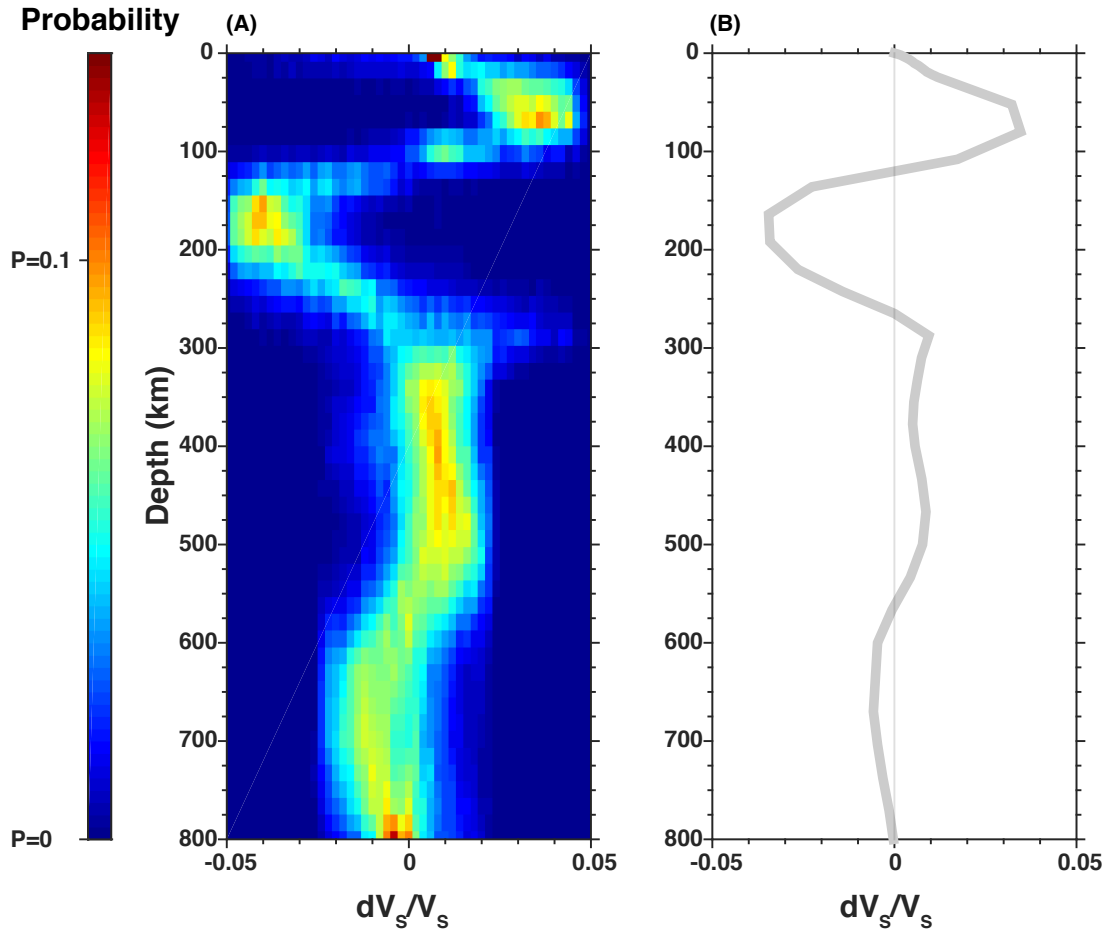


**Figure 15.** Posterior ensemble of solutions for the eastern Australia path. See Fig. 3 for details.

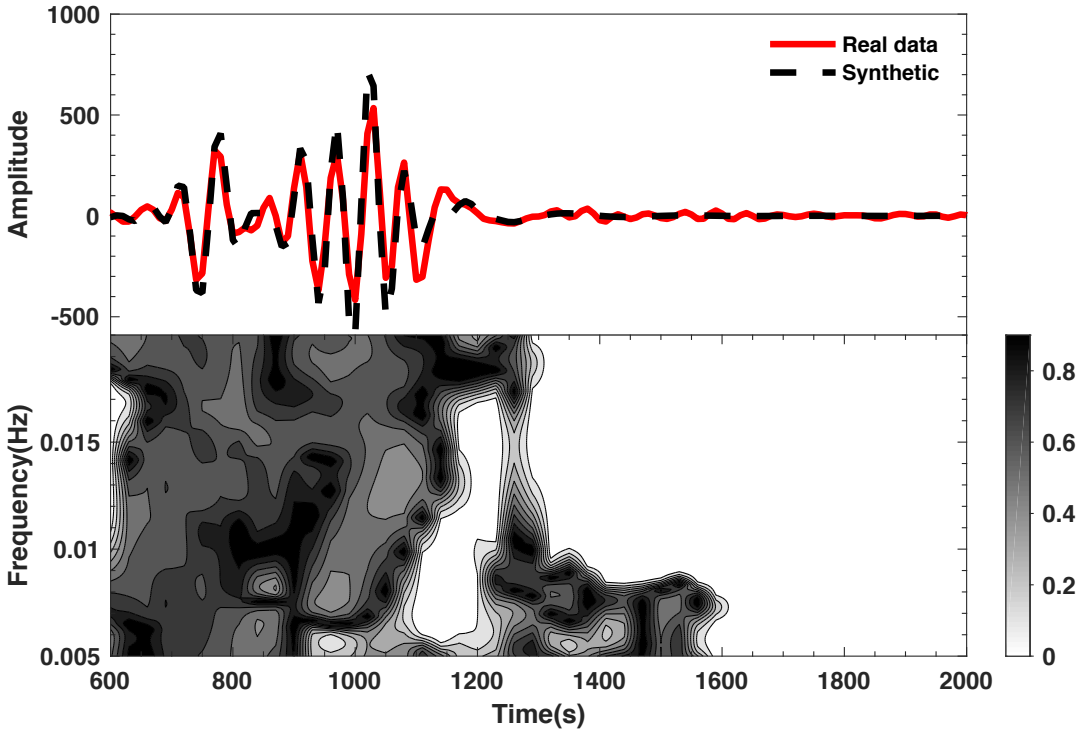


**Figure 16.** (A): real data and synthetic seismogram calculated using the inverted mean model of Figure 15; (B) F-T analysis of the misfit as defined in equation 16.

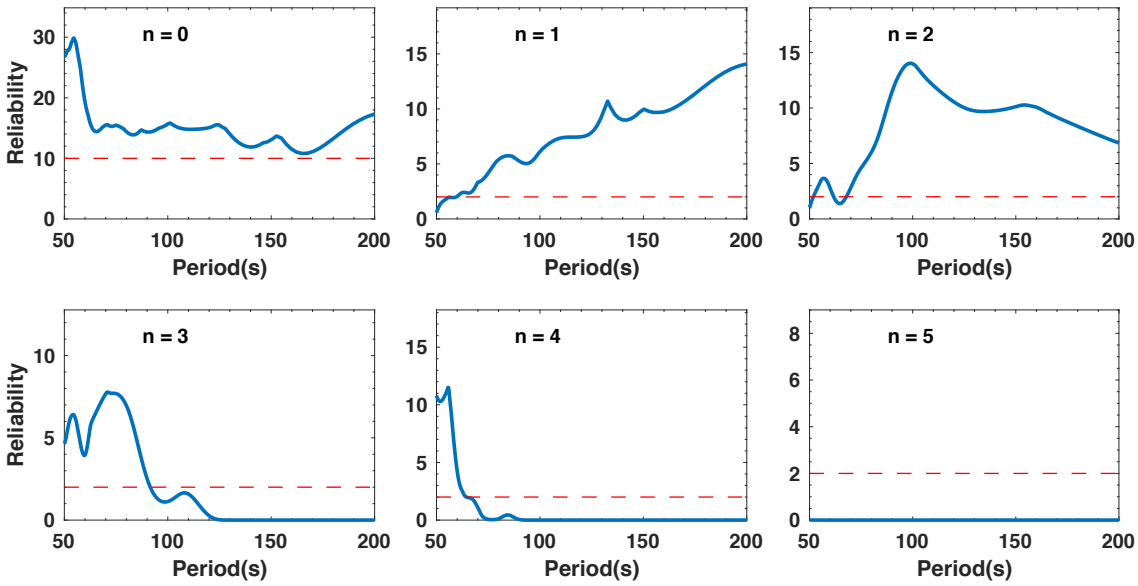


**Figure 17.** Reliabiliy test for the eastern Australia path. See Fig. 8 for details

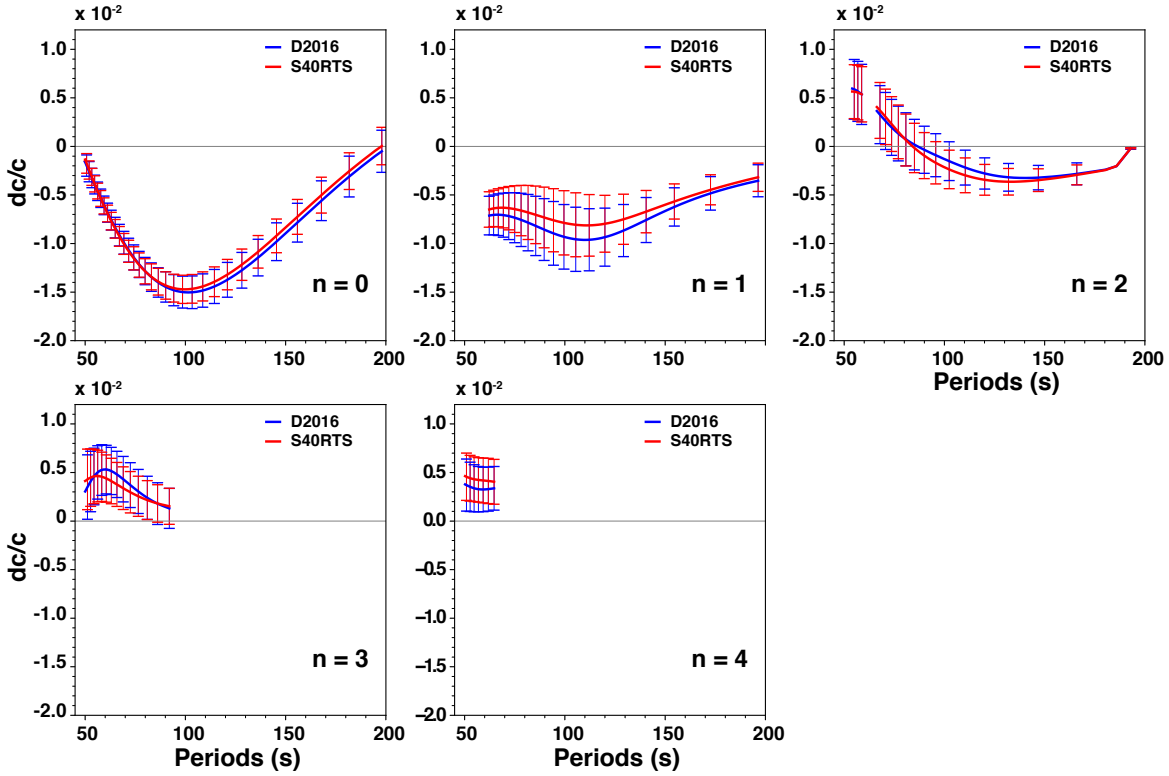


**Figure 18.** Reliable measured phase velocities expressed as perturbations with respect to PREM for the eastern Australia path and the modes and periods that were estimated to be reliable (Fig. 17). The red curve represents measurements performed using the model of Debayle et al. (2016) as a reference model. The blue curve are measurements performed using model S40RTS of Ritsema et al. (2011) as reference. The phase velocities were converted from perturbations with respect to the 3-D reference model into perturbations with respect to PREM. Uncertainties correspond to $1\sigma$.